

1 **Quantifying the migration rate of drainage divides from**
2 **high-resolution topographic data**

3 Chao Zhou¹, Xibin Tan^{2,*}, Yiduo Liu², Feng Shi^{1,3}

4 ¹ State Key Laboratory of Earthquake Dynamics, Institute of Geology, China
5 Earthquake Administration, Beijing 100029, China

6 ² Key Laboratory of Mountain Hazards and Surface Processes, Institute of Mountain
7 Hazards and Environment, Chinese Academy of Sciences, Chengdu 610299, China

8 ³ Shanxi Taiyuan Continental Rift Dynamics National Observation and Research
9 Station, Beijing 100029, China

10 *Corresponding author. E-mail address: tanxibin@imde.ac.cn

11 **Abstract**

12 The lateral movement of drainage divides is co-influenced by tectonics,
13 lithology, and climate, and therefore archives a wealth of geologic and climatic
14 information. It also has wide-ranging implications for topography, the sedimentary
15 record, and biological evolution, thus has drawn much attention in recent years.
16 Several methods have been proposed to determine drainage divides' migration state
17 (direction and rate), including geochronological approaches (e.g., ¹⁰Be) and
18 topography-based approaches (e.g., χ -plots or Gilbert metrics). A key object in these
19 methods is the channel head, which separates the hillslope and channel. However, due
20 to the limited resolution of topography data, the required channel-head parameters in
21 the calculation often cannot be determined accurately, and empirical values are used

22 in the calculation, which may induce uncertainties. Here, we propose two methods to
23 calculate the migration rate of drainage divides, based on the relatively accurate
24 channel-head parameters derived from high-resolution topographic data. We then
25 apply the methods to an active rift shoulder (Wutai Shan) in the Shanxi rift, and a
26 tectonically stable area (Yingwang Shan) in the Loess Plateau, to illustrate how to
27 calculate drainage-divide migration rates. Our results show that the Wutai Shan
28 drainage divide is migrating northwestward at a rate between 0.21 to 0.27 mm/yr,
29 whereas the migration rates at the Yingwang Shan are approximately zero. This study
30 indicates that the drainage-divide stability can be determined more accurately using
31 high-resolution topographic data. Furthermore, this study takes the cross-divide
32 differences in the uplift rate of channel heads into account in the measurement of
33 drainage-divide migration rate for the first time.

34 **Keywords**

35 Drainage divide; Migration rate; High-resolution topographic data; DEM; Channel
36 head

37 **1. Introduction**

38 The evolution of the Earth's surface is jointly controlled by tectonics, lithology,
39 and climatic conditions (e.g., Molnar and England, 1990; Whipple, 2009; Gallen,
40 2018; Bernard et al., 2021; Hoskins et al., 2023), providing a basis for reconstructing
41 the past tectonic (Pritchard et al., 2009; Kirby and Whipple, 2012; Shi et al., 2021) or

42 climatic processes (Tucker and Slingerland, 1997; Hancock et al., 2002; Schildgen et
43 al., 2022) through topography. The evolution of unglaciated terrestrial terrains is
44 fundamentally coupled with changes in drainage systems through river's vertical
45 (changes in river long profile) and lateral movements (drainage divide migration and
46 river captures) (Whipple, 2001; Clark et al., 2004; Bonnet, 2009; Willett et al., 2014).
47 Previous studies have extensively investigated how river channel profiles respond to
48 tectonic uplift (Whipple, 2001; Crosby and Whipple, 2006; Kirby and Whipple,
49 2012), lithological differences (Duvall et al., 2004; Safran et al., 2005; Forte et al.,
50 2016), and precipitation perturbations (Schlunegger et al., 2011; Bookhagen and
51 Strecker, 2012). River long profiles have been used to study earthquake events (e.g.,
52 Burbank and Anderson, 2001; Wei et al., 2015) and the spatio-temporal variations of
53 uplift (e.g., Whipple et al., 1999; Kirby et al., 2003; Pritchard et al., 2009; Goren et
54 al., 2014). Recent studies show that the widespread lateral movement of river basins
55 driven by geological and/or climatic disturbance (Yang et al., 2019; Zondervan et al.,
56 2020; Zhou et al., 2022a; Bian et al., 2024) also interacts with the adjustment of
57 channel profiles (Willett et al., 2014). Drainage-divide migration, one form of river
58 lateral movement, may not only carry information on geological and/or climatic
59 disturbance (Su et al., 2020; Zondervan et al., 2020; He et al., 2021; Shi et al., 2021;
60 Zhou et al., 2022a; Zeng and Tan, 2023) but also influence the extraction of tectonic
61 information from channel profiles (Goren et al., 2014; Ma et al., 2020; Jiao et al.,
62 2022). Moreover, it has multi-facet consequences for landscape evolution
63 (Scheingross et al., 2020; Stokes et al., 2023), sedimentary processes (Clift &

64 Blusztajn, 2005; Willett et al., 2018; Deng et al., 2020; Zhao et al., 2021), and
65 biological evolution (Waters et al., 2001; Zemplak et al., 2008; Hoorn et al., 2010;
66 Musher et al., 2021). For this reason, the stability of drainage divides has drawn more
67 and more attention in recent years (e.g., Authemayou et al., 2018; Vacherat et al.,
68 2018; Chen et al., 2021; Shelef and Goren, 2021; Sakashita and Endo, 2023; Bian et
69 al., 2024).

70 Drainage-divide migration is essentially controlled by the cross-divide
71 difference in erosion and topographic slope (Beeson et al., 2017; Dahlquist et al.,
72 2018; Chen et al., 2021; Zhou et al., 2022a). The erosion rates are routinely derived
73 from geochronological techniques, such as cosmogenic nuclides (e.g., ^{10}Be)
74 concentration measurements (Mandal et al., 2015; Struth et al., 2017; Young and
75 Hilley, 2018; Sassolas-Serrayet et al., 2019), which can be used to calculate the
76 migration rates of drainage divides (Beeson et al., 2017; Godard et al., 2019; Hu et al.,
77 2021). However, these techniques are usually based on samples collected from a
78 catchment outlet that is several, or even tens of, kilometers away from the drainage
79 divide and thus may not represent the erosion rates close to the drainage divide
80 (Sassolas-Serrayet et al., 2019; Zhou et al., 2022a). Besides, the high cost of sample
81 processing makes it challenging to determine the drainage divide's motion by
82 measuring the erosion rates throughout the large landscapes. Hence, it would be ideal
83 to find an accessible and efficient method that can be applied to the entire landscape
84 and make full use of the ^{10}Be -derived erosion rates.

85 The advancement of the digital elevation model (DEM) has promoted the

86 development of geomorphic analysis, making it possible to determine the drainage
87 divide's transient motion through topography analysis. For example, Willett et al.
88 (2014) applied the χ method to map the dynamic state of river basins. Forte and
89 Whipple (2018) proposed the cross-divide comparison of "Gilbert metrics" (including
90 channel heads' relief, slope, and elevation) to determine a drainage divide's migration
91 direction. Others adopted the comparison of slope angle or relief of the hillslopes
92 across a drainage divide to deduce its stability (Scherler and Schwanghart, 2020; Ye et
93 al., 2022; Zhou et al., 2022b). These geomorphic techniques, so far, could only
94 determine the migration direction of drainage divides. Braun (2018) provided an
95 equation that considers both alluvial and fluvial areas to calculate the migration
96 velocity of an escarpment (also a drainage divide). Zhou et al. (2022a) developed a
97 technique to calculate the migration rate through the high base-level χ values on both
98 sides of a drainage divide. These new approaches require channel-head parameters to
99 calculate the migration rate. However, the location of the channel heads sometimes
100 cannot be accurately identified because of the limitation in the resolution of DEMs in
101 natural cases. For this reason, empirical values of channel-head parameters are used in
102 these studies, which may induce uncertainties.

103 This study aims to establish an approach to derive the migration rate of drainage
104 divides, at a high precision and low cost, based on topographic analysis. We choose a
105 tectonically active area (i.e., the Wutai Shan in the Shanxi Rift) and a tectonically
106 inactive area (i.e., the Yingwang Shan in the Loess Plateau) to demonstrate how to
107 quantify drainage-divide migration rates (Fig. 1). We use the aerial photography

108 acquired by unmanned aerial vehicles (UAVs) and the Structure from Motion (SfM)
109 technology to obtain the high-resolution DEM data of these two areas (0.67 m and
110 0.84 m spatial resolution in the Wutai Shan and the Yingwang Shan, respectively).
111 Benefiting from the high-resolution data, the location of channel heads can be
112 identified more accurately. We then develop two methods to calculate the drainage-
113 divide migration rates. One is based on the measured channel-head parameters, and
114 the other is based on an improved method of Zhou et al (2022a). Combining with the
115 geological and low-temperature thermochronology studies of the Wutai Shan
116 (Middleton et al., 2017; Clinkscales et al., 2020), we also quantify the cross-divide
117 difference in uplift rates to improve the precision of drainage-divide migration rate.

118

119 **2. Methods**

120 **2.1 Channel-head-point method**

121 According to the detachment-limited stream power model (Howard and Kerby,
122 1983; Howard, 1994), the channel's erosion rate (E) can be expressed as:

$$123 \quad E = KA^mS^n \quad (1)$$

124 where K is the erosion coefficient, A is the upstream drainage area, S is the gradient of
125 the river channel, and m and n are empirical constants.

126 Because of thresholds such as erosion threshold (the shear stress of overland flow
127 must exceed the threshold of the cohesion of bed material to generate river incision)
128 (Howard and Kerby, 1983; Perron et al., 2008) or landslide threshold (landslides

129 occur when the threshold of soil or rock strength is exceeded in high relief region)
130 (Burbank et al., 1996; Tucker and Bras, 1998), river channels (following Eq. 1)
131 emerge at a certain distance from the drainage divide. The region between the channel
132 head and the drainage divide is referred to as the hillslope area, where the erosion is
133 controlled by landslide, collapse, and diffusion processes (Carson and Kirkby, 1972;
134 Stock and Dietrich, 2006; Stark, 2010; Braun et al., 2018; Dahlquist et al., 2018). The
135 channel-head point is the highest and the closest point to the drainage divide on a
136 river channel (Clubb et al., 2014). Therefore, the erosion rate at channel-head points
137 (E_{ch}) can be described as:

$$138 \quad E_{ch} = KA_{cr}^m S_{ch}^n \quad (2)$$

139 where E_{ch} is the erosion rate at channel-head points, A_{cr} is the critical upstream
140 drainage area of a channel-head point (Duvall et al., 2004; Wobus et al., 2006), and
141 S_{ch} is the channel-head gradient measured along the channel near the channel-head
142 point. Eq. 2 indicates that the side of a drainage divide with a higher A_{cr} or S_{ch} can
143 have a higher erosion rate than the other side, and is more likely to pirate the opposite
144 drainage basin. Besides, a high erosion coefficient can amplify the drainage basin's
145 erosion rate.

146 Drainage-divide migration is essentially controlled by the cross-divide difference
147 in erosion rates and topographic slope (Beeson et al., 2017; Dahlquist et al., 2018;
148 Chen et al., 2021; Zhou et al., 2022a; Stokes et al., 2023). Furthermore, the
149 differential uplift should also be considered when using the cross-divide erosion rates
150 at the channel heads to calculate the erosion difference across the divide, especially in

151 the case of tectonic tilting uplift (Zhou et al., 2022a). The drainage-divide migration
 152 rate (D_{mr}) can be obtained according to the cross-divide difference in erosion rate and
 153 uplift rate and the slopes across the divide (Zhou et al., 2022a):

$$154 \quad D_{mr} = \frac{\Delta E_{ch} - \Delta U_{ch}}{\tan\alpha + \tan\beta} \quad (3)$$

155 where ΔE_{ch} is the difference in erosion rate between the two sides (annotated as α and
 156 β) of the drainage divide ($\Delta E_{ch} = E_{cha} - E_{ch\beta}$). The choice of α or β is arbitrary, and the
 157 positive direction of the migration rate is assigned from the α to the β side whereas the
 158 negative is the opposite. ΔU_{ch} is the cross-divide difference in uplift rate ($\Delta U_{ch} = U_{cha}$
 159 $- U_{ch\beta}$), and $\tan\alpha$ and $\tan\beta$ are the average gradients (along the normal-divide
 160 direction) upslope of the channel head (not including the hilltop part) on the α side
 161 and the β side, respectively. Assuming the erosion coefficient (K) is the same on both
 162 sides of a drainage divide, Eqs. 2 and 3 allow us to derive the equation of drainage
 163 divide's migration rate according to the parameters at the channel-head points:

$$164 \quad D_{mr} = \frac{K[(A_{cr}^m S_{ch}^n)_\alpha - (A_{cr}^m S_{ch}^n)_\beta] - \Delta U_{ch}}{\tan\alpha + \tan\beta} \quad (4)$$

165 If the exact value of K is unknown, the drainage divide's unilateral erosion rate
 166 can be used as a substitution:

$$167 \quad D_{mr} = \frac{E_\alpha \left[1 - \frac{(A_{cr}^m S_{ch}^n)_\beta}{(A_{cr}^m S_{ch}^n)_\alpha} \right] - \Delta U_{ch}}{\tan\alpha + \tan\beta} \quad (5)$$

168 or:

$$169 \quad D_{mr} = \frac{E_\beta \left[\frac{(A_{cr}^m S_{ch}^n)_\alpha}{(A_{cr}^m S_{ch}^n)_\beta} - 1 \right] - \Delta U_{ch}}{\tan\alpha + \tan\beta} \quad (6)$$

170 E_α and E_β are the erosion rates of the α and the β side of the drainage divide,
 171 respectively, which can be derived through cosmogenic nuclides (^{10}Be) concentration

172 measurements (Beeson et al., 2017; Godard et al., 2019; Hu et al., 2021). The regional
 173 average erosion rate ($\bar{E} = \frac{E_\alpha + E_\beta}{2}$) can also be used to calculate the migration rate:

$$174 \quad D_{mr} = \frac{2\bar{E} \left[\frac{(A_{cr}^m S_{ch}^n)_\alpha - (A_{cr}^m S_{ch}^n)_\beta}{(A_{cr}^m S_{ch}^n)_\alpha + (A_{cr}^m S_{ch}^n)_\beta} \right] - \Delta U_{ch}}{\tan\alpha + \tan\beta} \quad (7)$$

175 Based on Eqs. 4-7, the migration rate of drainage divides can be estimated using
 176 channel-head parameters combined with one of the erosion-related parameters,
 177 erosion coefficient (K), erosion rate at one side of a drainage divide (E_α or E_β), or
 178 regional average erosion rate (\bar{E}).

179

180 2.2 Channel-head-segment method

181 A channel-head segment is the channel segment just below the channel head
 182 (Zhou et al., 2022a). Zhou et al. (2022a) developed a method based on the cross-
 183 divide χ contrast of channel-head segments to calculate the migration rate of drainage
 184 divides. The essence of the method is the cross-divide comparison of the channel-
 185 head segments' normalized channel steepness (k_{sn}) values. k_{sn} is a widely used index
 186 (Whipple et al., 1999; Wobus et al., 2006; Hilley and Arrowsmith, 2008; Kirby and
 187 Whipple, 2012) that is quantitatively related to E and K ($k_{sn} = \left(\frac{E}{K}\right)^{\frac{1}{n}}$). χ is an integral
 188 function ($\chi = \int_{x_b}^x \left(\frac{A_0}{A(x)}\right)^{\frac{m}{n}} dx$) of a channel's upstream area (A) to horizontal distance
 189 (x) (Royden et al., 2000; Perron and Royden, 2012), and A_0 is an arbitrary scaling area
 190 to make the integrand dimensionless.

191 In the method of Zhou et al. (2022a), the location of channel heads cannot be
 192 accurately identified, because it is limited by the resolution of DEM. Therefore, an

193 empirical value of $A_{cr} = 10^5 \text{ m}^2$ was used in the calculation. Benefiting from the high-
 194 resolution DEM in this study, we improve the method in Zhou et al. (2022a) and use
 195 the real location of channel heads to calculate the migration rate. When the regional
 196 erosion coefficient (K) is known and unchanged in the vicinity of the drainage divide,
 197 the drainage-divide migration rate can be estimated by the following equation:

$$198 \quad D_{mr} = \frac{K[k_{sn(\alpha)}^n - k_{sn(\beta)}^n] - \Delta U_{ch}}{\tan\alpha + \tan\beta} = \frac{K \left\{ \left[\frac{(z_{ch} - z_b)_\alpha}{\chi_\alpha} \right]^n - \left[\frac{(z_{ch} - z_b)_\beta}{\chi_\beta} \right]^n \right\} - \Delta U_{ch}}{\tan\alpha + \tan\beta} \quad (8)$$

199 where z_{ch} is the elevation of the channel head, z_b is the elevation of catchment outlet
 200 (at the top part of the channel to make the elevation- χ profiles quasi-linear between
 201 the channel head and the outlet), and subscripts α and β denote the two rivers across a
 202 divide. The detailed derivation of Eq. 8 is in Supplementary Materials. The drainage
 203 divide's unilateral erosion rate (E_α or E_β) can also be used as a substitution for the K
 204 value:

$$205 \quad D_{mr} = \frac{E_\alpha \left\{ 1 - \left(\frac{\chi_\alpha}{\chi_\beta} \right)^n \left[\frac{(z_{ch} - z_b)_\alpha}{(z_{ch} - z_b)_\beta} \right]^{-n} \right\} - \Delta U_{ch}}{\tan\alpha + \tan\beta} \quad (9)$$

206 or:

$$207 \quad D_{mr} = \frac{E_\beta \left\{ \left(\frac{\chi_\alpha}{\chi_\beta} \right)^{-n} \left[\frac{(z_{ch} - z_b)_\alpha}{(z_{ch} - z_b)_\beta} \right]^n - 1 \right\} - \Delta U_{ch}}{\tan\alpha + \tan\beta} \quad (10)$$

208 Alternatively, one can use the regional average erosion rate (\bar{E}) to calculate the
 209 migration rate:

$$210 \quad D_{mr} = \frac{2\bar{E} \left\{ \frac{\left[\frac{(z_{ch} - z_b)_\alpha}{(z_{ch} - z_b)_\beta} \right]^n - \left(\frac{\chi_\alpha}{\chi_\beta} \right)^n}{\left[\frac{(z_{ch} - z_b)_\alpha}{(z_{ch} - z_b)_\beta} \right]^n + \left(\frac{\chi_\alpha}{\chi_\beta} \right)^n} \right\} - \Delta U_{ch}}{\tan\alpha + \tan\beta} \quad (11)$$

211 Based on Eqs. 8-11, the drainage-divide migration rate can be estimated using the χ

212 values of high-base-level channel segments combined with one of the erosion-related
213 parameters, erosion coefficient (K), erosion rate at one side of a drainage divide (E_α or
214 E_β), or regional average erosion rate (\bar{E}).

215

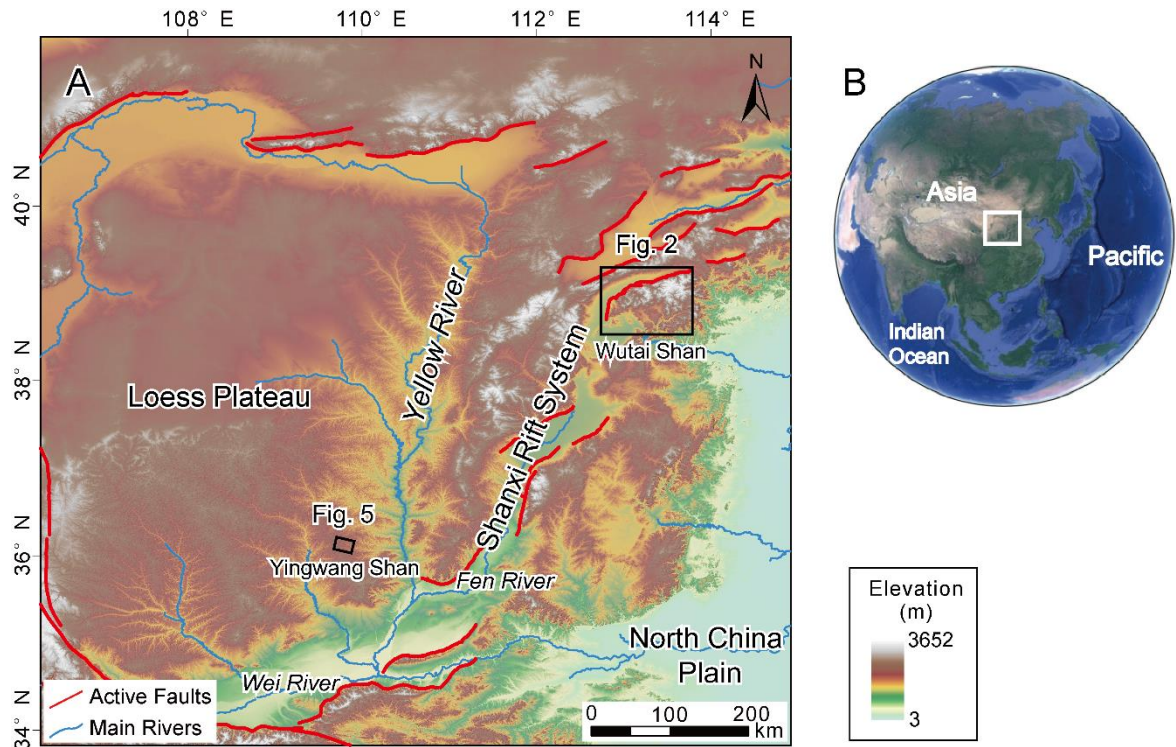
216 **2.3 Parameter extraction**

217 In this study, we apply the erosion coefficient (K) related equations (Eqs. 4 & 8)
218 to two natural examples in North China, the Wutai Shan in the Shanxi Rift and the
219 Yingwang Shan in the Loess Plateau, to demonstrate how to calculate the drainage-
220 divide migration rates (Fig. 1). We calculated the K , according to the equation, $K =$
221 $\frac{E}{k_{sn}^n}$, the erosion rate obtained by chronological methods, the k_{sn} , and the assumed
222 slope exponent ($n = 1$). The k_{sn} is calculated based on S and A ($k_{sn} = SA^{\frac{m}{n}}$) extracted
223 from ALOS DEM (downloaded from <https://search.asf.alaska.edu/>) using
224 TopoToolbox (Schwanghart and Scherler, 2014), and the interpolation uses the
225 Kriging method on ArcGIS (Fig. 2). We use a small four-rotor Unmanned Aerial
226 Vehicle (UAV), the DJI Phantom 4, to acquire stereo images of the areas. Based on
227 the Structure-from-Motion (SfM) method and PhotoScan software, we obtained the
228 DEMs with a spatial resolution of 0.67 m in the Wutai Shan and 0.84 m in the
229 Yingwang Shan (can be download from <https://doi.org/10.5069/G98C9TGT>). Both
230 regions are semi-arid, and the vegetation is dominated by shrubs. We did not compare
231 the elevations to the standard GPS points, which may bring errors on the elevations.

232 Based on the high-resolution topography data, we first extract river channels and

233 drainage divide, using a single-flow-direction algorithm (D8). Then we extract the
234 relevant parameters, and calculate the drainage-divide migration rate. Data analysis
235 including slope-area plots, χ -plots, river's long profiles and topographic swath
236 profiles, are based on the Matlab toolbox TAK (Forte and Whipple, 2019) and
237 TopoToolbox (Schwanghart and Scherler, 2014). According to the breaking point of
238 the slope-area regression line, we obtain the value of the critical upstream drainage
239 area (A_{cr}) of each river channel (Duvall et al., 2004). According to these values, we
240 mark the position (and its elevation, z_{ch}) of the channel heads on the χ -plots and the
241 topography map. An elevation of the catchment outlet (z_b) can be assigned at the top
242 part of the channel to make the elevation- χ profiles quasi-linear between the channel
243 head and the outlet. The slope of the channel head (S_{ch}) is calculated, according to the
244 100 m long channel on the river's long profiles around the channel head (50 m
245 upstream and downstream). Topographic gradient ($\tan\alpha$ or $\tan\beta$) is calculated through
246 the average slope (in the normal-divide direction) of the hillslope segment (not
247 including the hilltop part, because of its lower gradient). The cross-divide uplift
248 difference in the channel-head points (ΔU_{ch}) is estimated according to the location of
249 the each channel head and the tectonic uplift trend.
250

251 **3. Applications to natural cases**



252
253 **Figure 1.** Locations and tectonic background of the two nature cases in North China.

254 The figure is modified from Fig. 7 in Shi et al. (2021). (A) Red lines represent the
255 main active faults. Black rectangles show the locations of the two nature cases. Red
256 curve denotes active fault, sourced from <https://www.activefault-datacenter.cn/>. The
257 topography data (ALOS DEM) is downloaded from the Alaska Satellite Facility
258 (ASF) Data Search (<https://search.asf.alaska.edu/>). (B) The satellite image downloaded
259 from Google Earth. White rectangles show the location of Panel A.

260

261 **3.1 Wutai Shan**

262 The Wutai Shan is a tilted fault block on the shoulder of the Shanxi Rift System
263 located in the central North China craton (Fig. 1) (Xu et al., 1993; Su et al., 2021).

264 The tilting uplift of the Wutai Shan is controlled by the Northern Wutai Shan fault,
265 and there is no active fault along the south edge of the Wutai Shan horst (Fig. 2). The
266 bedrock of the Wutai Shan area consists mainly of metamorphic and igneous
267 basement rocks (Clinkscales et al., 2020) and there is no obvious variation in rock
268 erodibility and precipitation in this area (Fig. S2 & S3). Zhou et al. (2022b) reveal that
269 the Wutai Shan drainage divide is migrating northwestward due to the tilting uplift
270 and predicts the drainage divide will move ~10 km to the northwest to achieve a
271 steady state if all geological conditions remain. Geomorphic evidence also exhibits a
272 northwestward migration of the drainage divide (Fig. 3). The plan and satellite views
273 show several abnormally high junction angles around the Wutai Shan drainage divide,
274 which indicate that the tributaries formerly part of the northern drainage have become
275 part of the southern drainage (Fig. 3A&B). The χ -plots analysis shows the southern
276 side of the drainage divide has steeper channels, higher k_{sn} , and lower χ . The χ -plots
277 of paired rivers illustrate obvious characteristics of shrinking-expanding and captured-
278 beheaded rivers (Fig. 3C).

279 To derive the erosion coefficient of the Wutai Shan area, we calculate the
280 channel steepness (k_{sn}) of this region, assuming $n = 1$ and $m = 0.45$ (Wobus et al.,
281 2006; DiBiase et al., 2010; Perron and Royden, 2012; Wang et al., 2021). We then use
282 the Kriging interpolation method to generate the k_{sn} distribution map (Fig. 2B). In
283 addition, results under the assumptions of $m = 0.35$ and 0.55 , respectively, are shown
284 in Supplementary Materials (Fig. S4). The average k_{sn} value of the upthrown side near
285 the Northern Wutai Shan fault is $\sim 80 \text{ m}^{0.9}$ (Fig. 2D). Middleton et al. (2017) showed

286 that the Quaternary throw rates of the Northern Wutai Shan fault are 0.8-1.6 mm/yr.
287 Clinkscales et al. (2020) showed, using low-temperature thermochronology, that the
288 time-averaged long-term throw rates in the late Cenozoic is about 0.25 mm/yr, and
289 there is an accelerated activity in the Wutai Shan area. According to these studies, we
290 assume a 0.50 ± 0.25 mm/yr uplift/erosion rate in the northern margin of the Wutai
291 Shan (in the footwall of the Northern Wutai Shan fault). Combining with the equation,
292 $K = \frac{E}{k_{sn}n}$, and following the approach of previous studies (Kirby and Whipple, 2001;
293 Kirkpatrick et al., 2020; Ma et al., 2020), the erosion coefficient (K) is calculated to
294 be $(6.25 \pm 3.13) \times 10^{-6} \text{ m}^{0.1} \text{ yr}^{-1}$ in this area. Because there is no obvious variation in
295 rock erodibility and precipitation in this area (Figs. S2 & S3), we use this value as the
296 erosion coefficient (K) of the Wutai Shan area.

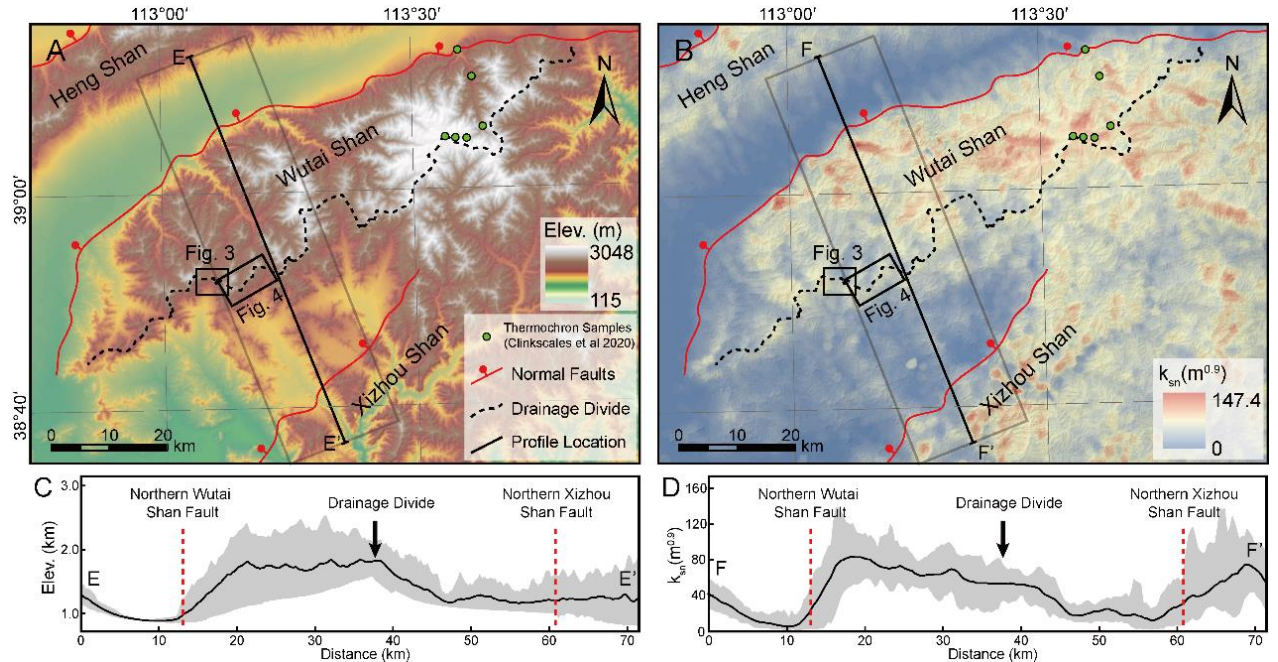
297 We then apply the two new methods (Eqs. 4 & 8) to calculate the migration rate
298 of the drainage divide in the Wutai Shan. We first choose three pairs of rivers (Fig.
299 4A) and acquire their slope-area plots (Figs. 4B, E, H) and the χ -plots (Figs. 4C, F, I).
300 According to the breaking point of the slope-area regression line (Duvall et al., 2004)
301 (Figs. 4B, E, H), we obtain the values of the critical upstream drainage area (A_{cr}).
302 According to these values, we separate hillslope and channel areas and mark the
303 position of the channel heads on the χ -plots and the topography map (Fig. 4A). For
304 the χ -plots (Figs. 4C, F, I), we obtain the elevations of channel heads (z_{ch}) and χ values
305 based on the coordinate of the channel-head points. According to the location of the
306 channel heads on the river's long profiles, we calculate the channel-head gradient
307 (S_{ch}). Topographic gradient ($\tan\alpha$ or $\tan\beta$) is calculated through the average slope (in

308 the normal-divide direction) of the hillslope segment (not including the hilltop part,
309 Figs. 4D, G, J).

310 According to the previous studies (Middleton et al., 2017; Clinkscales et al.,
311 2020) and the k_{sn} distribution (Fig. 2D), we assume the rock uplift rate decreases
312 linearly from 0.5 to 0 mm/yr from northwest to southeast of the Wutai Shan horst
313 (~40 km wide). Then we can obtain that the cross-divide uplift difference in the
314 channel-head points (ΔU_{ch}) (the distance perpendicular to the direction of the
315 boundary fault is ~600 m) is ~0.008 mm/yr. After determining these parameters, we
316 adopt the channel-head-point (Eq. 4) and channel-head-segment (Eq. 8) methods,
317 respectively, to calculate the migration rates. The required data for calculation and the
318 migration rates are shown in Table 1. The calculated results for $m/n = 0.35$ and 0.55 ,
319 respectively, are shown in Supplementary Materials (Table S1). The migration rates
320 are higher when $m/n = 0.35$ and lower when $m/n = 0.55$, which indicates the m/n value
321 is sensitive to the result.

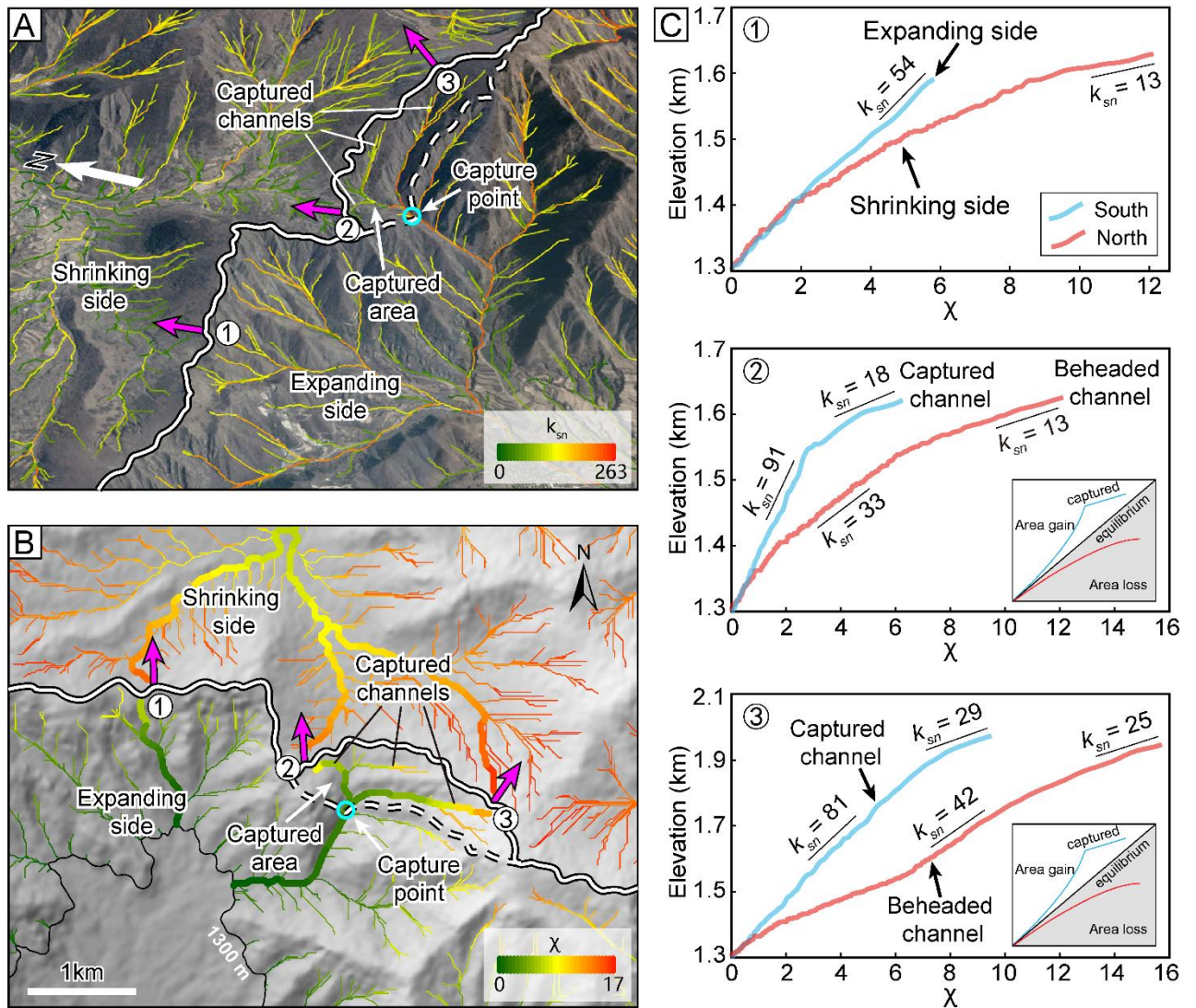
322 The rivers have different characteristics on both sides of the drainage divide, as
323 illustrated on their slope-area plots (Figs. 4B, E, H) and the χ -plots (Figs. 4C, F, I).
324 For the first site (Fig. 4D), the migration rates calculated by the channel-head-point
325 and channel-head-segment methods are 0.21 mm/yr and 0.26 mm/yr, respectively. For
326 the second site (Fig. 4G), the migration rates are 0.23 mm/yr and 0.27 mm/yr,
327 respectively. For the third site (Fig. 4J), 0.21 mm/yr and 0.22 mm/yr, respectively. The
328 drainage divides of all three points are migrating northwestward, which is consistent
329 with the previous result inferred by the cross-divide contrast of slopes in this area

330 (Zhou et al., 2022b). Furthermore, the migration rates calculated by the two methods
 331 are comparable in all three sites.
 332



333
 334 **Figure 2.** Topography (A) and normalized channel steepness (k_{sn}) (B) distribution of
 335 the Wutai Shan horst and surrounding area in the Shanxi Rift System. The black
 336 dashed line shows the location of the main drainage divide. Red lines show the main
 337 active faults. The black lines show the location of profiles E-E' and F-F'. Black
 338 rectangles show the area of Fig. 3B & 4A. Gray boxes show the area of the swath
 339 profiles in Panels C and D. Green dots denote the locations of the low-temperature
 340 thermochronology samples in Clinkscales et al. (2020). The k_{sn} is calculated based on
 341 S and A extracted from ALOS DEM ($k_{sn} = SA^{\frac{m}{n}}$) and a uniform m/n (0.45) using
 342 TopoToolbox (Schwanghart and Scherler, 2014), and the interpolation uses the
 343 Kriging method on ArcGIS. (C) Topography swath profile along E-E'. See location in
 344 Panel A. (D) k_{sn} swath profile along F-F'. See location in Panel B. The swath profiles

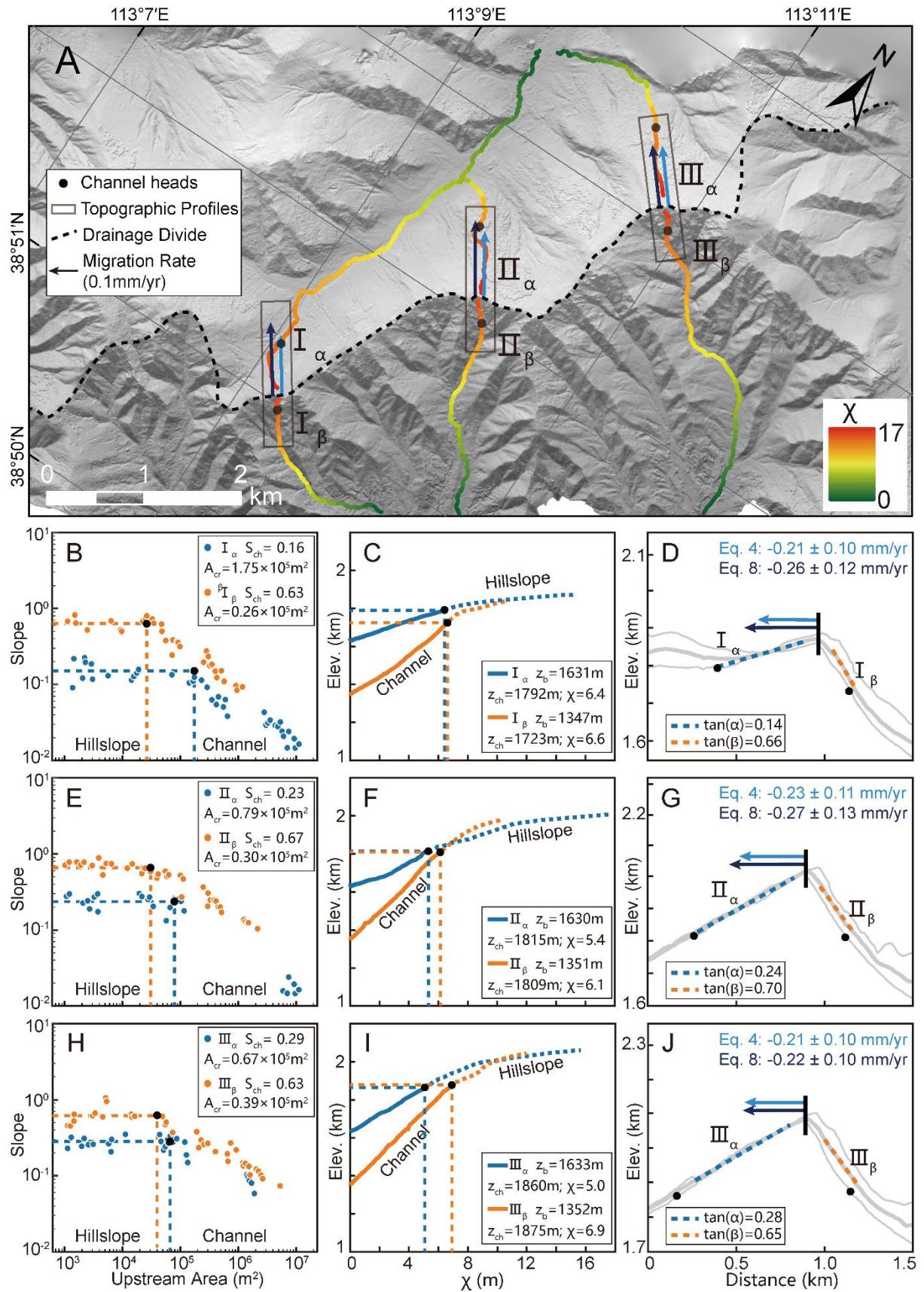
345 are extracted using TopoToolbox (Schwanghart and Scherler, 2014). The red dashed
 346 lines show the location of the main active normal faults, and the black arrow shows
 347 the location of the main drainage divide. Both swath profiles are 20 km wide (10 km
 348 on each side).
 349



350
 351 **Figure 3.** Perspective views and χ map of the drainage divide in the Wutai Shan (see
 352 Fig. 2 for location). (A) Perspective views of a captured area and the channels mapped
 353 with k_{sn} . The south side of the drainage divide has steeper channels and higher k_{sn} than
 354 the north side. Magenta arrows show drainage divide migration directions. The

355 satellite image is from Google Earth. (B) χ map of this area with the outlet elevation
356 of 1300 m. The south side of the drainage divide has lower χ values than the north
357 side. It should be noted that the catchment outlet at the north side of the drainage
358 basins (the 1300 m contour) is out of the map. The χ -plots of the rivers in bold lines
359 are shown in Panel C. (C) χ -plots of the three paired rivers in Panel B. The blue and
360 red curves correspond to the rivers on the south and north sides, respectively. The χ -
361 plot of River 1 is steeper on the south side, indicating that the river on the south side
362 is expanding and the river on the north side is shrinking. The χ -plots of Rivers 2 and 3
363 in the captured area show obvious characteristics of the captured and beheaded rivers.
364 The χ -plot is extracted using TAK (Forte and Whipple, 2019) and TopoToolbox
365 (Schwanghart and Scherler, 2014).

366



367

368 **Figure 4.** Analytical results of the Wutai Shan drainage divide. (A) High-resolution

369 hill-shade map (0.67 m spatial resolution) of the Wutai Shan. The black dashed line

370 shows the location of the main drainage divide. Colored lines show the three pairs of
371 selected channels used for analysis. The black dots are the channel heads. Black
372 rectangles show the location of the cross-divide topography swath profiles. The black
373 arrows show the direction of drainage-divide migration (**B, E, H**) Slope-area plots of
374 the three pairs of selected channels. The blue and orange dots are the slope-area plots
375 of the north (α) and south (β) sides of the drainage divide respectively. The black dots
376 represent the channel heads. (**C, F, I**) χ -plots of the selected channels. The blue and
377 orange lines are the χ -plots of the north (α) and south (β) sides of the drainage divide
378 respectively. The black dots represent the channel heads. (**D, G, J**) Cross-divide
379 topography swath profiles with the drainage-divide migration rates. The locations of
380 the profiles are in Panel A. The light and dark blue arrows are the drainage-divide
381 migration rates calculated by the channel-head-point (Eq. 4) and channel-head-
382 segment (Eq. 8) methods respectively.

383

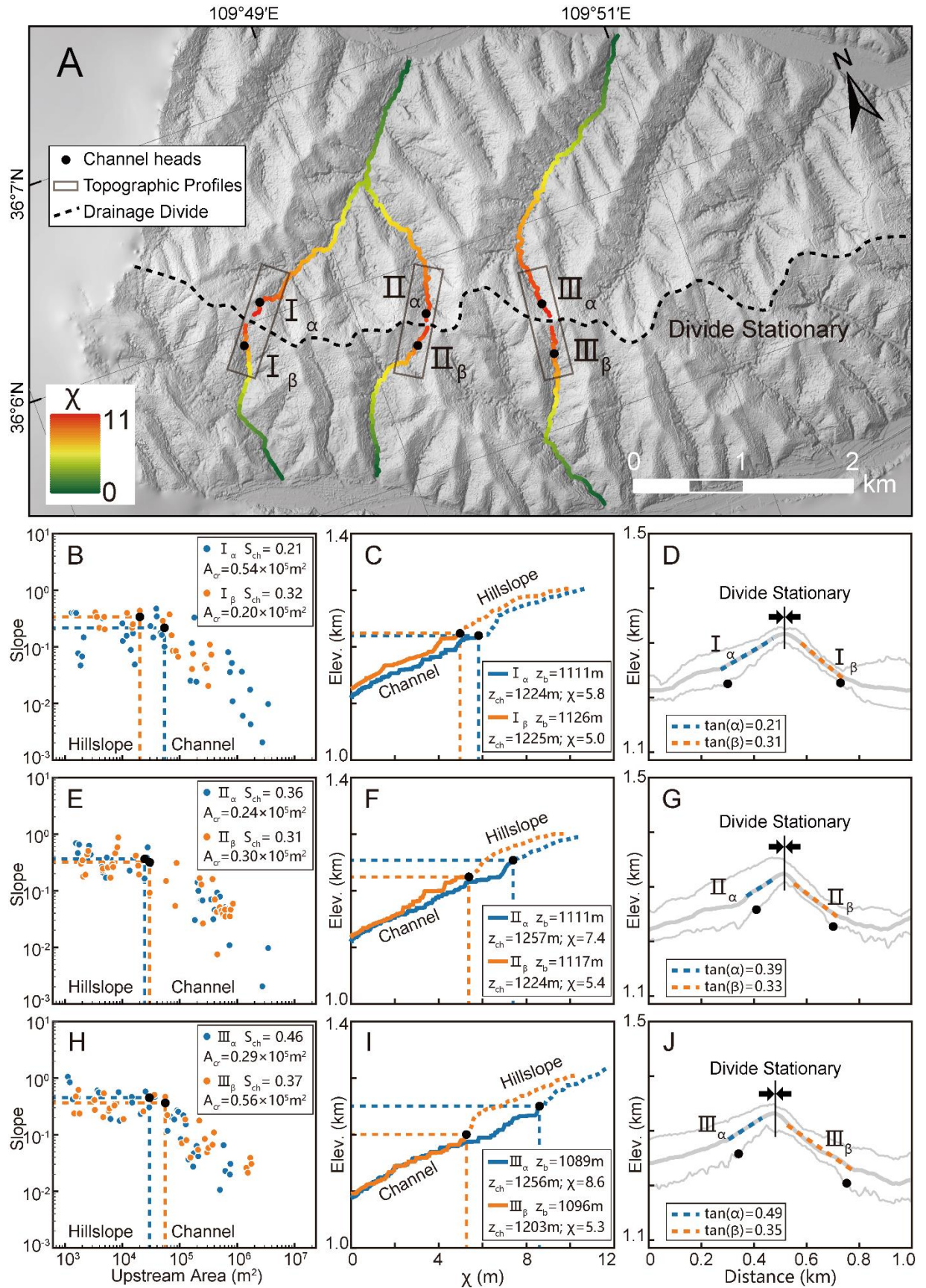
384 **3.2 Yingwang Shan**

385 The Loess Plateau is hosted by the tectonically stable Ordos Block of the North
386 China craton (Yin, 2010; Su et al., 2021). Over the past 2.6 million years, it has
387 accumulated tens to hundreds of meters of eolian sediments (Yan et al., 2014),
388 draping preexisting topography (Xiong et al., 2014). There is no active fault and little
389 to no variation in rock erodibility and precipitation within the area (Shi et al., 2020;
390 Zhou et al., 2022b).

391 We apply the two methods to Yingwang Shan of Loess Plateau to calculate the
392 drainage-divide migration rate. Similar to the Wutai Shan site, we obtain the slope-
393 area plots (Figs. 5 B, E, H), the χ -plots (Figs. 5 C, F, I), and extract the values of A_{cr} ,
394 S_{ch} , z_b , z_{ch} , γ , $\tan\alpha$ and $\tan\beta$ of the rivers. The rate of soil erosion in the study area is
395 about $500 \text{ t}\cdot\text{km}^{-2}\cdot\text{yr}^{-1}$ according to the distribution of silt discharge (Fu, 1989).
396 Combining with the assumption of the density of loess, $1.65 \text{ t}\cdot\text{m}^{-3}$, the present-day
397 erosion rate in the study area is calculated to be $0.3 \text{ mm}\cdot\text{yr}^{-1}$. Because there is no
398 obvious unequal uplift in this region, we assign that ΔU_{ch} is zero. We also assume $n =$
399 1 and $m = 0.45$ in the calculation (Wobus et al., 2006; DiBiase et al., 2010; Perron and
400 Royden, 2012; Wang et al., 2021). Then, we use the methods of channel-head
401 parameters (Eq. 7) and channel segments (Eq. 11) to calculate the drainage-divide
402 migration rates. The required data for calculation and the migration rates are shown in
403 Table 1.

404 All results of the three points show that the drainage-divide migration rate here is
405 close to zero, no matter which method is used in the calculation. The results show that
406 the drainage divide of the study site is in topographical equilibrium, which is
407 consistent with the inference in previous studies (Willett et al., 2014, Zhou et al.,
408 2022b).

409



410

411 **Figure 5.** Analytical results of the Yingwang Shan in the Loess Plateau. (A) High-

412 resolution hill-shade map (0.84 m spatial resolution). The black dotted line shows the
413 location of the main drainage divide. Colored lines show the three pairs of selected
414 channels used for analysis. The black dots represent the channel heads. Black
415 rectangles show the location of the cross-divide topography swath profiles. **(B, E, H)**
416 Slope-area plots of the three pairs of selected channels. The blue and orange dots are
417 the data of the north (α) and south (β) sides of the drainage divide respectively. The
418 black dots represent the channel heads. **(C, F, I)** χ -plots of the selected channels. The
419 blue and orange lines are the χ -plots of the north (α) and south (β) sides of the
420 drainage divide respectively. The black dots represent the channel heads. **(D, G, J)**
421 The cross-divide topography swath profiles. The locations of the swath profiles are in
422 Panel A.
423

Table 1. Channel parameters and migration rates of drainage divides in two field cases.

Natural Cases	No.	A_{cr} ($\times 10^5 \text{m}^2$)	S_{ch}	z_b (m)	z_{ch} (m)	χ	$\tan\alpha$	$\tan\beta$	ΔU_{ch} (mm/yr)	D_{mr} (mm/yr) (Channel-head-point method)	D_{mr} (mm/yr) (Channel-head-segment method)
Wutai Shan	Fig. 4 I α	1.75	0.16	1631	1792	6.4	0.14	0.66	~ 0.008	-0.21 ± 0.10	-0.26 ± 0.12
	Fig. 4 I β	0.26	0.63	1347	1723	6.6					
	Fig. 4 II α	0.79	0.23	1630	1815	5.4	0.24	0.70	~ 0.008	-0.23 ± 0.11	-0.27 ± 0.13
	Fig. 4 II β	0.30	0.67	1351	1809	6.1					
	Fig. 4 III α	0.67	0.29	1633	1860	5.0	0.28	0.65	~ 0.008	-0.21 ± 0.10	-0.22 ± 0.10
Fig. 4 III β	0.39	0.63	1352	1875	6.9						
Yingwang Shan	Fig. 5 I α	0.54	0.21	1111	1224	5.8	0.21	0.31	0	~ 0.03	~ -0.01
	Fig. 5 I β	0.20	0.32	1126	1225	5.0					
	Fig. 5 II α	0.24	0.36	1111	1257	7.4	0.39	0.33	0	~ 0.02	~ -0.01
	Fig. 5 II β	0.30	0.31	1117	1224	5.4					
	Fig. 5 III α	0.29	0.46	1089	1256	8.6	0.49	0.35	0	~ 0.02	~ -0.01
Fig. 5 III β	0.56	0.37	1096	1203	5.3						

426 **4. Discussion**

427 **4.1 Location of channel heads**

428 Willett et al. (2014) pioneered the use of cross-divide χ contrast to gauge the
429 horizontal motion of drainage divides. According to their method, drainage divides
430 are predicted to move toward the side with a higher χ value to achieve geomorphic
431 equilibrium. However, in a region with spatially variable uplift rates, lithology, or
432 precipitation, χ contrast may fail to reflect the drainage-divide migration (Willett et
433 al., 2014; Whipple et al., 2017; Forte and Whipple, 2018; Wu et al., 2022; Zhou and
434 Tan, 2023). In a tectonically active area, the cross-divide χ contrast can only be used
435 in a small area where rock type, precipitation, and uplift rate are nearly uniform
436 (Willett et al., 2014). Combining the advantages of the χ and Gilbert metrics methods,
437 Zhou et al. (2022a) proposed to use the χ contrast with a high base level to calculate
438 the k_{sn} values at the channel heads on both sides of a drainage divide, and quantified
439 the migration rate of drainage divides at the eastern margin of Tibet.

440 To reduce the cross-divide difference in uplift rate, precipitation, and rock
441 strength, the Gilbert metrics or χ -comparison method in Zhou et al. (2022a) should
442 compare the parameters of points (slope, relief, elevation, and k_{sn}) on both sides of the
443 divide as closely as possible. As the hillslope area (above the channel head) does not
444 follow Eq. 1 (Stock and Dietrich, 2006; Stark, 2010; Braun et al., 2018; Dahlquist et
445 al., 2018), the channel heads are the closest point to the divide, following Eq. 1.
446 Channel heads, therefore, are suitable for measuring the drainage-divide stability with

447 parameters of the upstream drainage area and channel gradient (Forte and Whipple,
448 2018; Zhou et al., 2022a). However, limited by the resolution of DEM, the location of
449 the channel heads cannot always be accurately identified. The channel head
450 parameters for calculating the migration rates are usually based on empirical values
451 (both sides are the same value) in previous studies (e.g., $A_{cr} = 10^5 \text{ m}^2$ in Zhou et al.
452 (2022a)), which may induce uncertainties.

453 In this study, we advocate the use of high-resolution DEM to determine a more
454 accurate position and related parameters of the channel head. The use of UAVs to
455 obtain the local DEM has become highly efficient. We advance the theory to calculate
456 the drainage-divide migration rate based on the measured channel-head parameters.
457 With the help of the aerial photography of UAVs and the SfM techniques, it is
458 possible to obtain the high-resolution topography data of drainage divides (Figs. 4A &
459 5A) and get the required parameters through topography analysis. The key parameters
460 includes the exact locations (usually have different A_{cr} across the divides) and the
461 gradients of the channel heads (S_{cr}), which could improve the quantitative research on
462 the drainage-divide migration. Furthermore, the method provides a new avenue to
463 combine with catchment-wide ^{10}Be erosion rate or low-temperature
464 thermochronology data to calculate the migration rate, which has great potential for
465 application in places where some variables are hard to be constrained.

466

467 **4.2 Cross-divide difference in the uplift rate of the channel heads**

468 Although the channel heads across the divide are very close on the spatial scale of
469 an orogenic belt, differential uplift between the channel heads (ΔU_{ch}) could still exist,
470 especially in a tilting horst, such as the Wutai Shan. The cross-divide difference in
471 uplift rate could impact the calculation of the migration rate of drainage divides (Zhou
472 et al., 2022a).

473 In this study, we quantify the influence of the cross-divide difference in rock
474 uplift rate (ΔU_{ch}) on the calculation of the migration rate of drainage divides at the
475 Wutai Shan, benefiting from the available tectonic and chronological research
476 (Clinkscales et al., 2020) and the newly obtained high-resolution topographic data. In
477 the Wutai Shan horst, ΔU_{ch} across the drainage divide is ~ 0.008 mm/yr. We estimate
478 the influence of ΔU_{ch} on the drainage-divide migration rate in this case study, which
479 can reduce the error theoretically. If ΔU_{ch} is ignored, the drainage-divide migration
480 rate would decrease by $\sim 4\%$ in the Wutai Shan case. Although $\sim 4\%$ seems to be
481 negligible, such a ratio will increase if the mountain belt is narrower, the tilting uplift
482 is stronger, or the divide is closer to the steady state (i.e., the migration rate is lower)
483 (Whipple et al., 2017; Ye et al., 2022). In other words, the differential uplift may play
484 a significant influence on the measurement of drainage-divide stability in some
485 situations. If we consider an extreme example where the main drainage divide of a
486 tilting mountain range (relatively narrow in width) is at a steady state, the gradient,
487 relief, and elevation of the channel heads (collectively called “Gilbert metrics”) (Forte
488 and Whipple, 2018) will show a systematic cross-divide difference in theory. In this

489 case, the drainage divide would be considered unstable if ΔU_{ch} were neglected.
490 Therefore, this study highlights that ΔU_{ch} should be taken into account, either in a
491 qualitative or a quantitative evaluation of the stability of drainage divides using the
492 parameters on the channel heads.

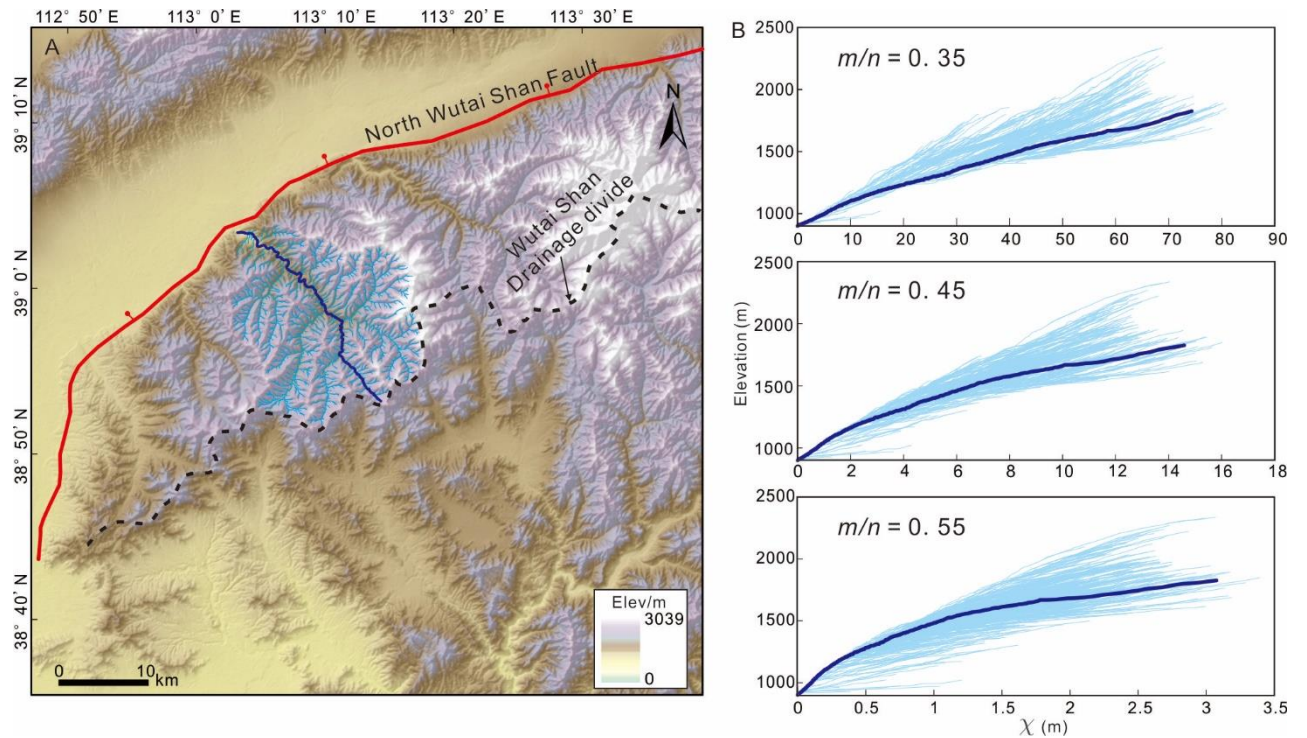
493

494 **4.3 Limitations and uncertainties**

495 This study develops the method to calculate the drainage-divide migration rate
496 based on the measured channel-head parameters. However, uncertainties still exist
497 because of the limitations of this technique. First, we assume the erosion coefficient
498 (K) is the same on both sides of a drainage divide in the derivation of the equations. If
499 there are differences in rock erodibility or precipitation across the divide, uncertainties
500 should exist in the results. Second, the calculation of migration rate is based on the
501 erosion rates at the channel area in this study. However, the occurrence of drainage-
502 divide migration is directly driven by the differential erosion of the hillslope area
503 across the divide, mainly via the processes including landslide, collapse, and diffusion
504 (Stock and Dietrich, 2006; Stark, 2010; Braun et al., 2018; Dahlquist et al., 2018).
505 Such discontinuous processes in the hillslope area make it challenging to constrain
506 erosion rates over such short timescales. Over a relatively longer period (i.e., spanning
507 multiple seismic and climatic cycles), the erosion rate at the channel head area in this
508 study can be comparable with that at the hillslope area (Hurst et al., 2012; Godard et
509 al., 2020).

510 The accuracy of the data and parameters can also impact the reliability of the

511 results. First, we use the uniform values of $n = 1$ and $m/n = 0.45$ in the two natural
512 cases to calculate the migration rate, because it is the best choice to align tributaries
513 with the main stem on the χ -plots in a drainage basin at the northern Wutai Shan (Fig.
514 6) (Perron and Royden, 2012). If the actual values deviate from the assumption, errors
515 would be introduced into the results. For this reason, we have added the cases of m/n
516 $= 0.35$ and 0.55 in Supplementary Materials. Further estimation of these values
517 (Mudd et al., 2018) could improve the accuracy of the results. Second, in the case of
518 the Wutai Shan, we refer to the geological and low-temperature thermochronology
519 studies and assume a 0.50 ± 0.25 mm/yr erosion rate at the northern margin of the
520 Wutai Shan (i.e., the footwall of the North Wutai Shan fault). Combining with the
521 present-day k_{sn} , we calculate the erosion coefficient (K) and derive the migration rates
522 of the drainage divide. If the present-day erosion rate deviates from the assumption,
523 errors would be inevitable in the results. Moreover, the horizontal and vertical errors
524 of the DEM data, as well as the calculation errors in slope, upstream area and channel
525 steepness can also affect the reliability of the results. In the case study of the
526 Yingwang Shan, the lush vegetation may bring errors to the DEM data based on the
527 SfM technology. The application of airborne light detection and ranging (LiDAR)
528 technology may help reduce this error. Future studies should take these challenges
529 into account and overcome them.



530

531 **Figure 6.** (A) Drainage basin in the northern Wutai Shan. (B) χ -plots of channel profiles
 532 in the drainage basin, using $A_0 = 1 \text{ m}^2$ and $m/n = 0.35, 0.45,$ and 0.55 . The χ -plots show
 533 the best choice of m/n is 0.45 , because the tributaries have systematically higher (m/n
 534 $= 0.35$) or lower ($m/n = 0.55$) elevations than the main stem for other values of m/n
 535 (excluding the channels in the headwaters).

536

537 **5. Conclusions**

538 We have developed a new method (called the "channel-head-point method") to
 539 calculate the migration rate of drainage divides based on channel-head parameters. We
 540 have also improved the previously proposed "channel-head-segment method" (Zhou
 541 et al., 2022a) to adapt the theory to areas where the parameters of channel-heads can
 542 be accurately determined.

543 Using the new methods and high-resolution topographic data, we determined the
544 exact locations of the channel heads on both sides of the drainage divide and
545 quantified the drainage-divide migration rates in two natural cases in North China:
546 Wutai Shan in the Shanxi Rift, and Yingwang Shan in the Loess Plateau. The
547 migration rates of the study sites in the Wutai Shan are 0.21-0.27 mm/yr
548 (northwestward). The rates are close to zero in the Yingwang Shan.

549 Based on the locations of the channel heads and the uplift gradient of the Wutai
550 Shan, we calculated the cross-divide difference in the uplift rate at the channel heads
551 (ΔU_{ch}), which is taken into account in the calculation of the drainage-divide migration
552 rate for the first time. If ΔU_{ch} is overlooked, the drainage-divide migration rate of the
553 study sites in the Wutai Shan will be underestimated by ~4%. Our study highlights
554 that ΔU_{ch} should be considered in the assessment of drainage divide stability based on
555 the cross-divide difference in channel-head parameters.

556

557 **Data availability.** The analysis of data is based on the Matlab toolbox TAK (Forte
558 and Whipple, 2019) and TopoToolbox (Schwanghart and Scherler, 2014). The
559 topography data (ALOS DEM) is downloaded from the Alaska Satellite Facility
560 (ASF) Data Search (<https://search.asf.alaska.edu/>). The high-resolution DEM of the
561 two study areas, the Wutai Shan and the Yingwang Shan, can be downloaded from
562 OpenTopography (<https://doi.org/10.5069/G98C9TGT>).

563 **Acknowledgements.** We would like to thank the Editor Simon Mudd, the
564 Reviewer Thomas Bernard, and an anonymous reviewer whose suggestions have

565 greatly improved the paper.

566 **Financial support.** This study is supported by the CAS Pioneer Hundred Talents
567 Program (E2K2010010) and the Fundamental Research Funds for the State Key
568 Laboratory of Earthquake Dynamics (LED2021A02).

569 **Competing interests.** The authors declare that they have no conflict of interest.

570 **Author contributions.** XT and CZ contributed to the design of the research
571 scheme. CZ performed the geomorphic analyses. CZ, XT, and FS carried out field
572 data collection. CZ, XT, YL, and FS contributed to the text and reviewed the paper.

573

574 **References**

- 575 Authemayou, C., Brocard, G., Delcaillau, B., Molliex, S., Pedoja, K., Husson, L.,
576 Aribowo, S., and Cahyarini, S. Y.: Unraveling the roles of asymmetric uplift,
577 normal faulting and groundwater flow to drainage rearrangement in an emerging
578 karstic landscape, *Earth Surface Processes and Landforms*, 43(9), 1885-1898,
579 <https://doi.org/10.1002/esp.4363>, 2018.
- 580 Beeson, H. W., McCoy, S. W., and Keen-Zebert, A.: Geometric disequilibrium of river
581 basins produces long-lived transient landscapes, *Earth Planet Sc. Lett.*, 475, 34-
582 43, <https://doi.org/10.1016/j.epsl.2017.07.010>, 2017.
- 583 Bernard, T., Sinclair, H. D., Gailleton, B., and Fox, M.: Formation of Longitudinal
584 River Valleys and the Fixing of Drainage Divides in Response to Exhumation of
585 Crystalline Basement, *Geophys. Res. Lett.*, 48,

586 <https://doi.org/10.1029/2020gl092210>, 2021.

587 Bian, S., Tan, X., Liu, Y., Fan, S., Gong, J., Zhou, C., Shi, F., and Murphy, M. A.:
588 Orographic rainfall drives the Himalaya drainage divide to move north,
589 *Geomorphology*, 108952, <https://doi.org/10.1016/j.geomorph.2023.108952>,
590 2024.

591 Bonnet, S.: Shrinking and splitting of drainage basins in orogenic landscapes from
592 the migration of the main drainage divide, *Nature Geoscience*, 2, 766-771,
593 <https://doi.org/10.1038/ngeo666>, 2009.

594 Bookhagen, B., and Strecker, M. R.: Spatiotemporal trends in erosion rates across a
595 pronounced rainfall gradient: Examples from the southern Central Andes, *Earth
596 Planet Sc. Lett.*, 327-328, 97-110, <https://doi.org/10.1016/j.epsl.2012.02.005>,
597 2012.

598 Braun, J.: A review of numerical modeling studies of passive margin escarpments
599 leading to a new analytical expression for the rate of escarpment migration
600 velocity, *Gondwana Research*, 53, 209-224,
601 <https://doi.org/10.1016/j.gr.2017.04.012>, 2018.

602 Burbank, D. W., Leland, J., Fielding, E., Anderson, R. S., Brozovic, N., Reid, M. R.,
603 and Duncan, C.: Bedrock incision, rock uplift and threshold hillslopes in the
604 northwestern Himalayas, *Nature*, 379, 505–510,
605 <https://doi.org/10.1038/379505a0>, 1996.

606 Burbank, D. W., and Anderson, R. S.: *Tectonic Geomorphology*, Blackwell Science,
607 Massachusetts p. 274, 2001.

608 Carson, M. A., and Kirkby, M. J.: Hillslope form and process, New York, Cambridge
609 University Press, 475, 1972.

610 Chen, C.-Y., Willett, S. D., Christl, M., and Shyu, J. B. H.: Drainage basin dynamics
611 during the transition from early to mature orogeny in Southern Taiwan, Earth
612 Planet Sc. Lett. 562, <https://doi.org/10.1016/j.epsl.2021.116874>, 2021.

613 Clark, M. K., Schoenbohm, L. M., Royden, L. H., Whipple, K. X., Burchfiel, B. C.,
614 Zhang, X., Tang, W., Wang, E., and Chen, L.: Surface uplift, tectonics, and
615 erosion of eastern Tibet from large-scale drainage patterns, Tectonics 23, 1-20,
616 <https://doi.org/10.1029/2002tc001402>, 2004.

617 Clift, P. D., and Blusztajn, J.: Reorganization of the western Himalayan river system
618 after five million years ago, Nature, 438, 1001-1003,
619 <https://doi.org/10.1038/nature04379>, 2005.

620 Clinkscales, C., Kapp, P., and Wang, H.: Exhumation history of the north-central
621 Shanxi Rift, North China, revealed by low-temperature thermochronology, Earth
622 Planet Sc Lett 536, 116146, <https://doi.org/10.1016/j.epsl.2020.116146>, 2020.

623 Clubb, F. J., Mudd, S. M., Milodowski, D. T., Hurst, M. D., and Slater, L. J.:
624 Objective extraction of channel heads from high-resolution topographic data,
625 Water Resources Research 50, 4283-4304,
626 <https://doi.org/10.1002/2013wr015167>, 2014.

627 Crosby, B. T., and Whipple, K. X.: Knickpoint initiation and distribution within
628 fluvial networks: 236 waterfalls in the Waipaoa River, North Island, New
629 Zealand, Geomorphology, 82, 16-38,

630 <https://doi.org/10.1016/j.geomorph.2005.08.023>, 2006.

631 Dahlquist, M. P., West, A. J., and Li, G.: Landslide-driven drainage divide migration,
632 *Geology*, 46, 403-406, <https://doi.org/10.1130/g39916.1>, 2018.

633 Deng, B., Chew, D., Mark, C., Liu, S., Cogné, N., Jiang, L., O’Sullivan, G., Li, Z.,
634 and Li, J.: Late Cenozoic drainage reorganization of the paleo-Yangtze river
635 constrained by multi-proxy provenance analysis of the Paleo-lake Xigeda, *GSA*
636 *Bulletin*, <https://doi.org/10.1130/b35579.1>, 2020.

637 DiBiase, R. A., Whipple, K. X., Heimsath, A. M., Ouimet, W. B.: Landscape form and
638 millennial erosion rates in the San Gabriel Mountains, CA, *Earth Planet Sc. Lett.*,
639 289, 134-144, <https://doi.org/10.1016/j.epsl.2009.10.036>, 2010.

640 Duvall, A.: Tectonic and lithologic controls on bedrock channel profiles and processes
641 in coastal California, *J. Geophys. Res.*, 109,
642 <https://doi.org/10.1029/2003jf000086>, 2004.

643 Forte, A. M., and Whipple, K. X.: Criteria and tools for determining drainage divide
644 stability, *Earth Planet Sc. Lett.*, 493, 102–117,
645 <https://doi.org/10.1016/j.epsl.2018.04.026>, 2018.

646 Forte, A. M., and Whipple, K. X.: Short communication: The Topographic Analysis
647 Kit (TAK) for TopoToolbox, *Earth Surface Dynamics* 7, 87–95,
648 <https://doi.org/10.5194/esurf-7-87-2019>, 2019.

649 Forte, A. M., Yanites, B. J., and Whipple, K. X.: Complexities of landscape evolution
650 during incision through layered stratigraphy with contrasts in rock strength,
651 *Earth Surface Processes and Landforms*, 41, 1736-1757,

652 <https://doi.org/10.1002/esp.3947>, 2016.

653 Fu, B.: Soil erosion and its control in the loess plateau of China, *Soil Use and*
654 *Management*, 5, 76-82, <https://doi.org/10.1111/j.1475-2743.1989.tb00765.x>,
655 1989.

656 Gallen, S. F.: Lithologic controls on landscape dynamics and aquatic species
657 evolution in post-orogenic mountains, *Earth Planet Sc. Lett.*, 493, 150-160,
658 <https://doi.org/10.1016/j.epsl.2018.04.029>, 2018.

659 Godard, V., Dosseto, A., Fleury, J., Bellier, O., and Siame, L.: Transient landscape
660 dynamics across the Southeastern Australian Escarpment, *Earth Planet Sc. Lett.*,
661 506, 397-406, <https://doi.org/10.1016/j.epsl.2018.11.017>, 2019.

662 Godard, V., Hippolyte, J.-C., Cushing, E., Espurt, N., Fleury, J., Bellier, O., and
663 Ollivier, V.: Hillslope denudation and morphologic response to a rock uplift
664 gradient, *Earth Surface Dynamics*, 8, 221-243, [https://doi.org/10.5194/esurf-8-](https://doi.org/10.5194/esurf-8-221-2020)
665 [221-2020](https://doi.org/10.5194/esurf-8-221-2020), 2020.

666 Goren, L., Fox, M., and Willett, S. D.: Tectonics from fluvial topography using formal
667 linear inversion: Theory and applications to the Inyo Mountains, California,
668 *Journal of Geophysical Research: Earth Surface*, 119, 1651-1681,
669 <https://doi.org/10.1002/2014jf003079>, 2014.

670 Hancock, G. S., and Anderson, R. S.: Numerical modeling of fluvial strath-terrace
671 formation in response to oscillating climate, *GSA Bulletin*, 114, 1131-1142,
672 [https://doi.org/10.1130/0016-7606\(2002\)114<1131:nmofst>2.0.co;2](https://doi.org/10.1130/0016-7606(2002)114<1131:nmofst>2.0.co;2), 2002.

673 He, C., Yang, C. J., Turowski, J. M., Rao, G., Roda-Boluda, D. C., and Yuan, X. P.:

674 Constraining tectonic uplift and advection from the main drainage divide of a
675 mountain belt, *Nat. Commun.*, 12, 544, [https://doi.org/10.1038/s41467-020-](https://doi.org/10.1038/s41467-020-20748-2)
676 [20748-2](https://doi.org/10.1038/s41467-020-20748-2), 2021.

677 Hilley, G. E., and Arrowsmith, J. R.: Geomorphic response to uplift along the
678 Dragon's Back pressure ridge, Carrizo Plain, California, *Geology*, 36,
679 <https://doi.org/10.1130/g24517a.1>, 2008.

680 Young, H. H., and Hilley, G. E.: Millennial-scale denudation rates of the Santa Lucia
681 Mountains, California: Implications for landscape evolution in steep, high-relief,
682 coastal mountain ranges, *GSA Bulletin*, 130 (11-12), 1809–1824,
683 <https://doi.org/10.1130/B31907.1>, 2018.

684 Hoorn, C., Wesselingh, F. P., Steege, H. T., Bermudez, M. A., and Antonelli, A.:
685 Amazonia Through Time: Andean Uplift, Climate Change, Landscape Evolution,
686 and Biodiversity, *Science*, 330, 927-931,
687 <https://doi.org/10.1126/science.1194585>, 2010.

688 Hoskins, A. M., Attal, M., Mudd, S. M., and Castillo, M.: Topographic Response to
689 Horizontal Advection in Normal Fault-Bound Mountain Ranges, *Journal of*
690 *Geophysical Research: Earth Surface*, 128,
691 <https://doi.org/10.1029/2023jf007126>, 2023.

692 Howard, A. D., Dietrich, W. E., and Seidl, M. A.: Modeling fluvial erosion on
693 regional to continental scales, *Journal of Geophysical Research: Solid Earth*, 99,
694 13971-13986, <https://doi.org/10.1029/94jb00744>, 1994.

695 Howard, A. D., and Kerby, G.: Channel changes in badlands, *Geological Society of*

696 America Bulletin, 94, 739, <https://doi.org/10.1130/0016->
697 [7606\(1983\)94<739:CCIB>2.0.CO;2](https://doi.org/10.1130/0016-7606(1983)94<739:CCIB>2.0.CO;2), 1983.

698 Hu, K., Fang, X., Ferrier, K. L., Granger, D. E., Zhao, Z., and Ruetenik, G. A.:
699 Covariation of cross-divide differences in denudation rate and χ : Implications for
700 drainage basin reorganization in the Qilian Shan, northeast Tibet, Earth Planet
701 Sc. Lett., 562, 116812, <https://doi.org/10.1016/j.epsl.2021.116812>, 2021.

702 Hurst, M. D., Mudd, S. M., Walcott, R., Attal, M., and Yoo, K.: Using hilltop
703 curvature to derive the spatial distribution of erosion rates, Journal of
704 Geophysical Research: Earth Surface, 117,
705 <https://doi.org/10.1029/2011jf002057>, 2012.

706 Jiao, R., Fox, M., and Yang, R.: Late Cenozoic erosion pattern of the eastern margin
707 of the Sichuan Basin: Implications for the drainage evolution of the Yangtze
708 River, Geomorphology, 398, 108025,
709 <https://doi.org/10.1016/j.geomorph.2021.108025>, 2022.

710 Kirby, E., and Whipple, K.: Quantifying differential rock-uplift rates via stream
711 profile analysis, Geology, 29, 415-418, <https://doi.org/10.1130/0091->
712 [7613\(2001\)029<0415:Qdrurv>2.0.Co;2](https://doi.org/10.1130/0091-7613(2001)029<0415:Qdrurv>2.0.Co;2), 2001.

713 Kirby, E., Whipple, K., Tang, W., and Chen, Z.: Distribution of active rock uplift
714 along the eastern margin of the Tibetan Plateau: Inferences from bedrock channel
715 longitudinal profiles, Journal of Geophysical Research, 108(B4), 2217,
716 <https://doi.org/10.1029/2001JB000861>, 2003.

717 Kirby, E., and Whipple, K. X.: Expression of active tectonics in erosional landscapes,

718 J. Struct. Geol., 44, 54-75, <https://doi.org/10.1016/j.jsg.2012.07.009>, 2012.

719 Kirkpatrick, H. M., Moon, S., Yin, A., and Harrison, T. M.: Impact of fault damage on
720 eastern Tibet topography, *Geology*, 48, <https://doi.org/10.1130/g48179.1>, 2020.

721 Ma, Z., Zhang, H., Wang, Y., Tao, Y., and Li, X.: Inversion of Dadu River Bedrock
722 Channels for the Late Cenozoic Uplift History of the Eastern Tibetan Plateau,
723 *Geophys. Res. Lett.*, 47, <https://doi.org/10.1029/2019gl086882>, 2020.

724 Mandal, S. K., Lupker, M., Burg, J.-P., Valla, P. G., Haghypour, N., and Christl, M.:
725 Spatial variability of ¹⁰Be-derived erosion rates across the southern Peninsular
726 Indian escarpment: A key to landscape evolution across passive margins, *Earth
727 Planet Sc. Lett.*, 425, 154-167, <https://doi.org/10.1016/j.epsl.2015.05.050>, 2015.

728 Molnar, P., and England, P.: Late Cenozoic uplift of mountain ranges and global
729 climate change: chicken or egg? *Nature*, 346, 29-34,
730 https://doi.org/10.1038_346029a0, 1990.

731 Mudd, S. M., Clubb, F. J., Gailleton, B., and Hurst, M. D.: How concave are river
732 channels? *Earth Surface Dynamics*, 6, 505-523, [https://doi.org/10.5194/esurf-6-
733 505-2018](https://doi.org/10.5194/esurf-6-505-2018), 2018.

734 Musher, L. J., Giakoumis, M., Albert, J., Rio, G. D., Rego, M., Thom, G., Aleixo, A.,
735 Ribas, C. C., Brumfield, R. T., and Smith, B. T.: River network rearrangements
736 promote speciation in lowland Amazonian birds, Cold Spring Harbor Laboratory,
737 <https://doi.org/10.1126/sciadv.abn1099>, 2021.

738 Perron, J. T., Dietrich, W. E., and Kirchner, J. W.: Controls on the spacing of first-
739 order valleys, *J. Geophys. Res.*, 113, <https://doi.org/10.1029/2007jf000977>,

740 2008.

741 Perron, J. T., and Royden, L.: An integral approach to bedrock river profile analysis,
742 Earth Surface Processes and Landforms, 38, 570-576,
743 <https://doi.org/10.1002/esp.3302>, 2012.

744 Pritchard, D., Roberts, G. G., White, N. J., and Richardson, C. N.: Uplift histories
745 from river profiles, Geophys. Res. Lett., 36,
746 <https://doi.org/10.1029/2009gl040928>, 2009.

747 Royden, L., Clark, M., and Whipple, K.: Evolution of river elevation profiles by
748 bedrock incision: Analytical solutions for transient river profiles related to
749 changing uplift and precipitation rates, Eos Trans, AGU, 81, 2000.

750 Safran, E. B., Bierman, P. R., Aalto, R., Dunne, T., Whipple, K. X., and Caffee, M.:
751 Erosion rates driven by channel network incision in the Bolivian Andes, Earth
752 Surface Processes and Landforms, 30, 1007-1024,
753 <https://doi.org/10.1002/esp.1259>, 2005.

754 Sassolas-Serrayet, T., Cattin, R., Ferry, M., Godard, V., and Simoes, M.: Estimating
755 the disequilibrium in denudation rates due to divide migration at the scale of
756 river basins, Earth Surface Dynamics, 7, 1041-1057,
757 <https://doi.org/10.5194/esurf-7-1041-2019>, 2019.

758 Scheingross, J. S., Limaye, A. B., McCoy, S. W., and Whittaker, A. C.: The shaping of
759 erosional landscapes by internal dynamics, Nature Reviews Earth &
760 Environment, 1, 661-676, <https://doi.org/10.1038/s43017-020-0096-0>, 2020.

761 Scherler, D., and Schwanghart, W.: Drainage divide networks – Part 2: Response to

762 perturbations, *Earth Surface Dynamics*, 8, 261-274,
763 <https://doi.org/10.5194/esurf-8-261-2020>, 2020.

764 Schildgen, T. F., van der Beek, P. A., D'Arcy, M., Roda-Boluda, D., Orr, E. N., and
765 Wittmann, H.: Quantifying drainage-divide migration from orographic rainfall
766 over geologic timescales: Sierra de Aconquija, southern Central Andes, *Earth*
767 *Planet Sc. Lett.*, 579, 117345, <https://doi.org/10.1016/j.epsl.2021.117345>, 2022.

768 Schlunegger, F., Norton, K. P., and Zeilinger, G.: Climatic Forcing on Channel
769 Profiles in the Eastern Cordillera of the Coroico Region, Bolivia, *The Journal of*
770 *Geology*, 119, 97-107, <https://doi.org/10.1086/657407>, 2011.

771 Schwanghart, W., and Scherler, D.: Short Communication: TopoToolbox 2 –
772 MATLAB-based software for topographic analysis and modeling in Earth
773 surface sciences, *Earth Surface Dynamics*, 2, 1-7, [https://doi.org/10.5194/esurf-](https://doi.org/10.5194/esurf-2-1-2014)
774 [2-1-2014](https://doi.org/10.5194/esurf-2-1-2014), 2014.

775 Shelef, E., and Goren, L.: The rate and extent of wind-gap migration regulated by
776 tributary confluences and avulsions, *Earth Surface Dynamics*, 9(4), 687-700,
777 <https://doi.org/10.5194/esurf-9-687-2021>, 2021.

778 Shi, F., Tan, X., Zhou, C., and Liu, Y.: Impact of asymmetric uplift on mountain
779 asymmetry: Analytical solution, numerical modeling, and natural examples,
780 *Geomorphology*, 389, 107862, <https://doi.org/10.1016/j.geomorph.2021.107862>,
781 2021.

782 Shi, W., Dong, S., and Hu, J.: Neotectonics around the Ordos Block, North China: A
783 review and new insights, *Earth-Science Reviews*, 200, 102969,

784 <https://doi.org/10.1016/j.earscirev.2019.102969>, 2020.

785 Stark, C. P.: Oscillatory motion of drainage divides, *Geophys. Res. Lett.*, 37,

786 <https://doi.org/10.1029/2009gl040851>, 2010.

787 Stock, J. D., and Dietrich, W. E.: Erosion of steepland valleys by debris flows,

788 *Geological Society of America Bulletin*, 118, 1125-1148,

789 <https://doi.org/10.1130/b25902.1>, 2006.

790 Stokes, M. F., Larsen, I. J., Goldberg, S. L., McCoy, S. W., Prince, P. P., and Perron, J.

791 T.: The Erosional Signature of Drainage Divide Motion Along the Blue Ridge

792 Escarpment, *Journal of Geophysical Research: Earth Surface*, 128,

793 <https://doi.org/10.1029/2022jf006757>, 2023.

794 Struth, L., Teixell, A., Owen, L. A., and Babault, J.: Plateau reduction by drainage

795 divide migration in the Eastern Cordillera of Colombia defined by morphometry

796 and ^{10}Be terrestrial cosmogenic nuclides, *Earth Surface Processes and*

797 *Landforms*, 42, 1155-1170, <https://doi.org/10.1002/esp.4079>, 2017.

798 Su, P., He, H., Tan, X., Liu, Y., Shi, F., and Kirby, E.: Initiation and Evolution of the

799 Shanxi Rift System in North China: Evidence From Low-Temperature

800 Thermochronology in a Plate Reconstruction Framework, *Tectonics*, 40,

801 <https://doi.org/10.1029/2020tc006298>, 2021.

802 Su, Q., Wang, X., Lu, H., and Xie, H.: Dynamic Divide Migration as a Response to

803 Asymmetric Uplift: An Example from the Zhongtiao Shan, North China, *Remote*

804 *Sensing*, 12, <https://doi.org/10.3390/rs12244188>, 2020.

805 Tucker, G. E., and Bras, R. L.: Hillslope processes, drainage density, and landscape

806 morphology, *Water Resources Research*, 34, 2751-2764,
807 <https://doi.org/10.1029/98wr01474>, 1998.

808 Tucker, G. E., and Slingerland, R.: Drainage basin responses to climate change, *Water*
809 *Resources Research*, 33, 2031-2047, <https://doi.org/10.1029/97wr00409>, 1997.

810 Vacherat, A., Bonnet, S., and Mouthereau, F.: Drainage reorganization and divide
811 migration induced by the excavation of the Ebro basin (NE Spain), *Earth Surface*
812 *Dynamics*, 6(2), 369-387, <https://doi.org/10.5194/esurf-6-369-2018>, 2018.

813 Wang, Y., Liu, C., Zheng, D., Zhang, H., Yu, J., Pang, J., Li, C., and Hao, Y.:
814 Multistage Exhumation in the Catchment of the Anninghe River in the SE
815 Tibetan Plateau: Insights From Both Detrital Thermochronology and
816 Topographic Analysis, *Geophys. Res. Lett.*, 48,
817 <https://doi.org/10.1029/2021gl092587>, 2021.

818 Waters, J. M., Craw, D., Youngson, J. H., and Wallis, G. P.: Genes meet geology: fish
819 phylogeographic pattern reflects ancient, rather than modern, drainage
820 connections, *Evolution*, 55, 1844-1851, [https://doi.org/10.1111/j.0014-](https://doi.org/10.1111/j.0014-3820.2001.tb00833.x)
821 [3820.2001.tb00833.x](https://doi.org/10.1111/j.0014-3820.2001.tb00833.x), 2001.

822 Wei, Z., Arrowsmith, J. R., and He, H.: Evaluating fluvial terrace riser degradation
823 using LiDAR-derived topography: An example from the northern Tian Shan,
824 China, *Journal of Asian Earth Sciences*, 105, 430-442,
825 <https://doi.org/10.1016/j.jseaes.2015.02.016>, 2015.

826 Whipple, K. X.: Fluvial landscape response time: how plausible is steady-state
827 denudation? *Am. J. Sci.*, 301, 313-325, <https://doi.org/10.2475/ajs.301.4-5.313>,

828 2001.

829 Whipple, K. X.: The influence of climate on the tectonic evolution of mountain belts,
830 Nature Geoscience, 2, 97-104, <https://doi.org/10.1038/ngeo413>, 2009.

831 Whipple, K. X., Forte, A. M., DiBiase, R. A., Gasparini, N. M., and Ouimet, W. B.:
832 Timescales of landscape response to divide migration and drainage capture:
833 Implications for the role of divide mobility in landscape evolution, Journal of
834 Geophysical Research: Earth Surface, 122, 248-273,
835 <https://doi.org/10.1002/2016JF003973>, 2017.

836 Whipple, K. X., Kirby, E., and Brocklehurst, S. H.: Geomorphic limits to climate-
837 induced increases in topographic relief, Nature, 401, 39-43,
838 <https://doi.org/10.1038/43375>, 1999.

839 Willett, S. D., McCoy, S. W., Perron, J. T., Goren, L., and Chen, C. Y.: Dynamic
840 reorganization of river basins, Science, 343, 1117,
841 <https://doi.org/10.1126/science.1248765>, 2014.

842 Willett, S. D., McCoy, S. W., and Beeson, H. W.: Transience of the North American
843 High Plains landscape and its impact on surface water, Nature, 561, 528-532,
844 <https://doi.org/10.1038/s41586-018-0532-1>, 2018.

845 Wobus, C., Whipple, K. X., Kirby, E., Snyder, N., Johnson, J., Spyropolou, K.,
846 Crosby, B., and Sheehan, D.: Tectonics from topography: Procedures, promise,
847 and pitfalls, Tectonics, Climate, and Landscape Evolution, 55-74,
848 [https://doi.org/10.1130/2006.2398\(04\)](https://doi.org/10.1130/2006.2398(04)) , 2006.

849 Wu, Y., Yang, R., He, C., and He, J.: Caution on determining divide migration from

850 cross-divide contrast in χ , *Geological Journal*, 57(12),
851 <https://doi.org/10.1002/gj.4530>, 2022.

852 Xiong, L.-Y., Tang, G.-A., Li, F.-Y., Yuan, B.-Y., and Lu, Z.-C.: Modeling the
853 evolution of loess-covered landforms in the Loess Plateau of China using a DEM
854 of underground bedrock surface, *Geomorphology*, 209, 18-26.
855 <https://doi.org/10.1016/j.geomorph.2013.12.009>, 2014.

856 Xu, X., Ma, X., and Deng, Q.: Neotectonic activity along the Shanxi rift system,
857 China, *Tectonophysics*, 219, 305-325, [https://doi.org/10.1016/0040-
858 1951\(93\)90180-R](https://doi.org/10.1016/0040-1951(93)90180-R), 1993.

859 Yan, M.-J., He, Q.-Y., Yamanaka, N., and Du, S.: Location, Geology and Landforms
860 of the Loess Plateau, in: Tsunekawa, A., Liu, G., Yamanaka, N., Du, S. (Eds.),
861 Restoration and development of the degraded Loess Plateau, China, Springer
862 Japan, 3-22, <https://doi.org/10.1007/978-4-431-54481-4>, 2014.

863 Yang, R., Suhail, H. A., Gourbet, L., Willett, S. D., Fellin, M. G., Lin, X., Gong, J.,
864 Wei, X., Maden, C., Jiao, R., and Chen, H.: Early Pleistocene drainage pattern
865 changes in Eastern Tibet: Constraints from provenance analysis,
866 thermochronometry, and numerical modeling, *Earth Planet Sc. Lett.*, 531, 1-10,
867 <https://doi.org/10.1016/j.epsl.2019.115955>, 2019.

868 Ye, Y., Tan, X., and Zhou, C.: Initial topography matters in drainage divide migration
869 analysis: Insights from numerical simulations and natural examples,
870 *Geomorphology*, 409, 108266, <https://doi.org/10.1016/j.geomorph.2022.108266>,
871 2022.

872 Yin, A.: Cenozoic tectonic evolution of Asia: A preliminary synthesis, *Tectonophysics*
873 488, 293-325, <https://doi.org/10.1016/j.tecto.2009.06.002>, 2010.

874 Zemplak, T. S., Habit, E. M., Walde, S. J., Battini, M. A., Adams, E. D. M., and
875 Ruzzante, D. E.: Across the southern Andes on fin: glacial refugia, drainage
876 reversals and a secondary contact zone revealed by the phylogeographical signal
877 of *Galaxias platei* in Patagonia, *Molecular Ecology*, 17, 5049-5061,
878 <https://doi.org/10.1111/j.1365-294X.2008.03987.x>, 2008.

879 Zeng, X., and Tan, X.: Drainage divide migration in response to strike-slip faulting:
880 An example from northern Longmen Shan, eastern Tibet, *Tectonophysics*, 848,
881 229720, <https://doi.org/10.1016/j.tecto.2023.229720>, 2023.

882 Zhao, X., Zhang, H., Hetzel, R., Kirby, E., Duvall, A.R., Whipple, K. X., Xiong, J.,
883 Li, Y., Pang, J., Wang, Y., Wang, P., Liu, K., Ma, P., Zhang, B., Li, X., Zhang, J.,
884 and Zhang, P.: Existence of a continental-scale river system in eastern Tibet
885 during the late Cretaceous-early Palaeogene, *Nat. Commun.*, 12, 7231,
886 <https://doi.org/10.1038/s41467-021-27587-9>, 2021.

887 Zhou, C., Tan, X., Liu, Y., Lu, R., Murphy, M. A., He, H., Han, Z., and Xu, X.:
888 Ongoing westward migration of drainage divides in eastern Tibet, quantified
889 from topographic analysis, *Geomorphology*, 402, 108123,
890 <https://doi.org/10.1016/j.geomorph.2022.108123>, 2022a.

891 Zhou, C., Tan, X., Liu, Y., and Shi, F.: A cross-divide contrast index (C) for assessing
892 controls on the main drainage divide stability of a mountain belt,
893 *Geomorphology*, 398, 108071, <https://doi.org/10.1016/j.geomorph.2021.108071>,

894 2022b.

895 Zhou, C., and Tan, X.: Quantifying the influence of asymmetric uplift, base level
896 elevation, and erodibility on cross-divide χ difference, *Geomorphology*, 427,
897 108634, <https://doi.org/10.1016/j.geomorph.2023.108634>, 2023.

898 Zondervan, J. R., Stokes, M., Boulton, S. J., Telfer, M. W., and Mather, A. E.: Rock
899 strength and structural controls on fluvial erodibility: Implications for drainage
900 divide mobility in a collisional mountain belt, *Earth Planet Sc. Lett.*, 538,
901 <https://doi.org/10.1016/j.epsl.2020.116221>, 2020.